RSC Advances

PAPER

View Article Online
View Journal | View Issue

Cite this: *RSC Adv.*, 2025, **15**, 34322

A highly sensitive photoelectrochemical immunosensor for cancer antigen (CA 125) based on a nanoplatform of carbon dots and cadmium sulphide

Ezinne U. Ekwujuru, Cornelius C. Ssemakalu, Michael J. Klink and Moses G. Peleyeju *

The prognosis for ovarian cancer is often poor due to late diagnosis. This is because the disease rarely presents with any specific symptoms in the early stage. There is therefore a need to develop a sensitive device for the routine screening of CA 125, the most widely used biomarker for detecting and monitoring ovarian malignancy. Herein, we report the development of a photoelectrochemical (PEC) immunosensor based on a screen-printed carbon electrode (SPCE) modified with a carbon nanodot/cadmium sulphide (CND/CdS) heterostructure for the sensitive detection of CA 125. Using a drop-casting technique and a self-assembly process, the immunosensor was constructed by the successive immobilization of CND, CdS, an *N*-hydroxysuccinimide/1-ethyl-3-(3-dimethylaminopropyl)carbodiimide (NHS–EDC) complex, anti-CA 125, and the blocking agent bovine serum albumin (BSA) on the SPCE. CND and CdS nanoparticles provided adequate surface area for electrochemical processes and served as photoactive materials, working synergistically to amplify signals and enhance the sensitivity of the sensor. The NHS–EDC complex activated the carboxyl groups on the modified electrode and served as a linker for antibody attachment. Under optimized conditions, the developed PEC immunosensor exhibited good sensitivity, selectivity, repeatability and reproducibility for CA 125 over a linear range of 100–0.0001 μg mL^{-1}, with a detection limit of 2.7 pg mL^{-1}. It also showed excellent short- and long-term stability and successfully detected CA 125 in serum samples. The excellent performance of the biosensor makes it a potential diagnostic tool for the real-time detection of CA 125 and other physiologically important analytes.

Received 24th July 2025
Accepted 3rd September 2025

DOI: 10.1039/d5ra05359e

rsc.li/rsc-advances

1 Introduction

Ovarian cancer (OC) is a malignant disease that affects the ovaries, fallopian tubes and primary peritoneal cavity, and it poses a huge global health burden.[1,2] It is the seventh most occurring female-related malignancy worldwide but has the highest mortality-to-case ratio among all gynecological cancers.[1,3] With about 239 000 cases and 152 000 mortalities yearly, OC prevalence is predicted to increase sharply by 2040.[1,3] Late detection, caused by non-specific symptoms and the lack of proper screening, makes treatment difficult.[1,4] Therefore, early diagnostic devices are crucial to improve treatment outcomes.

Traditional diagnostic approaches, such as pelvic examinations and transvaginal ultrasonography, are performed on symptomatic patients, leading to late diagnosis.[5] CA 125, a biomarker highly associated with OC, is valuable for early detection.[6] Its levels are elevated in about 90% of OC patients[7] and in 50–60% of those with early-stage disease.[8,9] However, its lack of specificity to OC makes it more useful as an initial screening measure.[10]

CA 125 detection has been carried out using immunoassays such as enzyme-linked immunosorbent assay and radioimmunoassay, which provide high specificity.[11] However, they are costly, complex, time-consuming, and require technical expertise.[12] These methods are also unreliable in detecting early-stage ovarian cancer biomarkers at low levels, further stressing the need for a highly reliable, cost-effective, non-invasive, and point-of-care diagnostic tool.[1,11,12]

Photoelectrochemical (PEC) immunosensing is a modern, advanced assay that uses light irradiation coupled with electrochemical methods for the sensitive detection of analytes.[13,14] The excitation source, which is separated from detection signals, helps reduce undesirable background noise, thereby enhancing its sensitivity and enabling low detection limits.[13,14] In addition to this, PEC systems are easy to operate, less expensive and easily miniaturized.[15] The PEC system normally consists of a working electrode modified with semiconductors

Department of Natural Sciences, Vaal University of Technology, Vanderbijlpark 1911, South Africa. E-mail: mosesp@vut.ac.za; mgpeleyeju@gmail.com

that are photoactive, coupled with a reference and counter electrode.[16,17] A light source of medium wavelength is used for irradiation.[18,19] When a certain voltage is applied to the working electrode, a photocurrent is generated, which varies with time. The change in photocurrent correlates with the analyte concentration.[14] PEC analysis to a large extent depends on the photoactive materials, typically, semiconductors, which serve as light-harvesting material to generate signals and as substrate for the immobilization of biomolecules.[20] Semiconductors are employed in PEC sensing due to their ability to generate charge carriers upon light irradiation, enabling effective detection.[21] The ideal semiconductors should exhibit biocompatibility to maintain the integrity of biomolecules and the sensor as a whole while providing mechanical stability to ensure accurate and reliable sensing.[22,23]

PEC sensing is relatively new; however, a few reports have been published on PEC sensors for CA 125. Wang *et al.* developed a PEC biosensor for CA 125 on a platform of a heterostructured material comprising CdS, Bi_2S_2 and NiS. The synergistic interaction of these materials led to a low limit of detection (LOD) of 0.85 pg mL^{-1} and a wide linear detection range of 1 pg mL^{-1} to 50 ng mL^{-1}.[24] To achieve a more sensitive platform for CA 125 sensing, sandwich-type PEC systems have also been developed. Xue and colleagues utilized core–shell SiO_2 nanoparticles and CdTe QDs as photoactive materials to detect CA 125. The PEC immunosensor produced an ultralow LOD of 0.3 mU mL^{-1} with a linear concentration range of 1 mU mL^{-1} to 100 U mL^{-1}.[25] Similarly, Zou *et al.* employed a CuO–ZnO heterojunction as a signal source with near-zero background noise in a sandwich PEC sensing platform for CA 125. The platform detected CA 125 in the range of 1×10^5 to 100 U mL^{-1} and an LOD of 3.16 U mL^{-1}.[26] In short, photoactive materials employed for the construction of a PEC biosensor have a huge influence on the sensitivity of the sensor.[27,28] This work utilised a combination of CdS and carbon nanodots (CNDs) to exploit their unique properties in the development of a PEC sensor for CA 125.

Cadmium sulphide is a semiconductor that has received tremendous attention over the years due to its unique properties, which include a narrow band gap of 2.42 eV, low potential oxidation, high electrical conductivity and low production cost.[29,30] CdS is also biocompatible and is well-known for its high quantum confinement effects and high electron mobility.[31] CdS nanoparticles possess high surface-to-volume ratio that promotes electroactivity and improves the loading of biomolecules.[32,33] Despite these excellent properties, CdS has the problem of photogenerated electron and hole recombination.[29] Adding other semiconductors or doping with metals can improve photoelectric conversion efficacy and enhance charge transfer.[29,34]

Carbon nanodots (CNDs) are zero-dimensional with a quasi-spherical shape. They are biocompatible and exhibit good electrical conductivity, a large surface-to-volume ratio, excellent tunability, chemical stability and high water solubility.[35,36] They have excellent electronic and optical properties, with high photostability and photocatalytic properties.[37,38] Their optical properties that have attracted scientists includes chemiluminescence, electro-chemiluminescence, size-dependent photoluminescence, up-conversion luminescence, and photo-induced electron transfer.[39] In addition, CNDs have a wide range of light absorption spectra, basically in the UV and visible light regions.[35,40] The band-edge position permits electron transfer from the surface of semiconductors, promoting charge separation, thereby blocking recombination.[41,42]

Reports on the use of CdS and CND composite as an immobilization layer for cancer antibodies are limited.[43] It has however been used for the sensitive detection of chromium (VI) ions.[43] It was able to detect ions within a dynamic range of 2–120 μM with a low detection limit of 2.07 μM. The heterostructure has also been employed in the detection of the organic compound benzaldehyde over a range of 0.1 nM to 1.0 mM, with an ultralow LOD of 2.2 ± 0.1 pM.[44]

In this work, a heterostructure of CdS and CND was used to construct a new, sensitive PEC immunosensor for CA 125 detection. The synergistic interaction between the nanomaterials significantly enhanced the sensitivity of the immunosensor.

2 Experimental

2.1 Fabrication of the PEC immunosensor

2.1.1 Preparation of SPCE/Carbon nanodot electrode. To prepare the CND-modified screen-printed carbon electrode (SPCE), 2–10 mg of CND was dispersed in 1 mL of dimethyl formamide (DMF) and ultrasonicated for 1 h. Thereafter, 5 μL of the dispersion was drop-casted onto the bare SPCE surface and then allowed to air-dry at room temperature.[45] The modified electrode was denoted as SPCE/CND.

2.1.2 Preparation of SPCE/carbon nanodots/CdS electrode. The SPCE/CND/CdS electrode was prepared by drop-casting 5 μL of a dispersion of CdS NPs (containing 10 mg of CdS NPs in 1 mL of DMF) onto the surface of the previously prepared SPCE/CND electrode. The resulting electrode was then allowed to dry at room temperature to enhance self-assembly of the particles.[46]

2.1.3 Antibody immobilization on SPCE/CND/CdS electrode. The SPCE/CND/CdS electrode was modified with 5 μL of a solution containing 20 mM EDC and 10 mM NHS in a 2 : 1 ratio of ethanol and PBS. This was allowed to incubate for 30 min according to a modified method of Hayat *et al.*[47] The EDC-NHS complex activates the carboxylate groups on the SPCE/CND/CdS electrode and serves as a crosslinker for the antibody.[47,48] Ethanol was used to improve the solubility of the EDC-NHS complex and facilitate the crosslinking process.[49] However, ethanol can denature proteins and impair the ability of antibodies to bind to antigens, thereby negatively impacting the output signal.[50,51] Hence, after the immobilization of the complex, the electrode was left to dry at room temperature (to vaporize the ethanol), and prior to immobilization of the antibody, it was rinsed with PBS (pH 7.4) to remove any residual ethanol. Subsequently, 5 μL of a 10 μg per mL CA 125 antibody solution, freshly dissolved in 1 mL of 10 mM PBS (pH 7.4), was applied to the electrode and incubated for 30 min to allow for covalent bonding with the activated carboxyl group on the surface of the modified electrode. Unattached antibody was

washed with PBS (pH 7.4). Thereafter, the electrode was incubated with 5 μL of 1% BSA for 20 min. Excess BSA was removed by washing with 100 μL of PBS. The electrode was allowed to dry at room temperature. The fabricated immunosensors were then incubated with varying concentrations of CA 125 antigen, ranging from 100 to 0.00001 μg mL^{-1}. A diagrammatic representation of the fabrication process and the electron transfer mechanism are presented in Fig. 3 and 4 respectively in the SI.

3 Results and discussion

3.1 Fourier transform infrared spectroscopy of CdS and CND

The FTIR spectrum of CdS in Fig. S5 shows many vibrational peaks that are similar to those in the literature.[52,53] The band at ~618 cm^{-1} is assigned to Cd–S stretching vibrations, which confirms the successful synthesis of the nanomaterial.[52–54] Vibrational bands at 1636 cm^{-1} and 3480 cm^{-1} represent OH bending and O–H stretching vibrations of absorbed water on the surface of CdS.[54] The FTIR spectrum of CNDs (Fig. S5) displays peaks at ~3065, 1558, 1012, and 779 cm^{-1}, corresponding to O–H stretching vibrations of carboxylic acids; C=O and C=C stretching vibrations; and C–H vibrations, respectively. This result is consistent with the findings reported in other works.[45,55,56]

3.2 Ultraviolet-visible spectroscopy of CdS and CND

The UV-vis absorption spectra of the synthesized CND and CdS NPs are shown in Fig. S6. The peaks at 276 nm, 347 nm and 414 nm are characteristic of CNDs, with its high energy tail extending further into the visible region. This indicates the presence of excited electrons.[55] The absorption band positions of CNDs can be affected by the starting materials and the synthesis method.[57] The peak at around 276 nm comes from the π–π* energy transition of conjugated C=C bonds, which indicates the presence of aromatic π-system in the core of the CNDs. The absorption peak at 347 nm represents the n–π* energy transition of C=O bonds, which originates from the surface of the CNDs.[55,57,58] The peak at around 414 nm is assigned to n–π* energy transitions of functional groups on the carbon dot surfaces.[58] These peaks yield strong fluorescence emission as a result of the excited state energy trapping by surface states.[55]

The broad absorption band of CdS NPs at 498 nm indicates that their electrons are excited in the visible light region and is similar to those reported in the literature.[59,60] The absorption spectrum of the nanocomposite maintained the peaks of the individual components with a well-defined broad peak in the visible light region.

3.3 X-ray diffraction patterns of CdS and CND

XRD patterns of the synthesized materials are shown in Fig. S7. The patterns of CdS NPs show strong diffraction peaks at 26.5°, 30.6°, 43.9°, 51.9° and 54.5°, corresponding to the *hkl* planes of (111), (200), (220), (311) and (222), respectively.[61] These peaks indicate a cubic crystal structure. The XRD pattern of CNDs shows broad peaks from ~16.6° to 24.9° with low intensity, which reveals an amorphous phase.[62] The XRD pattern of the nanocomposite maintained the strong diffraction peaks of CdS NPs. Peak identification was carried out using the Joint Committee on Powder Diffraction Standards (JCPDS) card no. 01-075-1546.

The average crystallite size of CdS NPs was obtained using the Debye–Scherrer formula.[61]

$$D = K\lambda/\beta \cos\theta, \quad (1)$$

where D: crystallite size; K: Scherrer's constant = 0.9; λ: wavelength of Cu Kα radiation (λ = 1.54060 Å); β: full width at half maximum (FWHM); θ: Bragg's angle.

The average crystallite size was calculated to be 3.7 nm, which differs from the particle size calculated from TEM (8.477 nm). This difference was as anticipated because of the agglomeration of particles observed in the TEM image (Fig. S8b).

3.4 Transmission electron microscopy analysis of CdS and CND

The TEM images of the synthesized CNDs, CdS NPs and their composite are shown in Fig. S8. The TEM image of the carbon nanodots (Fig. S8a) shows small, quasi-spherical particles. CNDs are known to have zero dimension and are quasi-spherical in shape.[63,64] The TEM image of CdS NPs (Fig. S8b) shows aggregates of fine, spherical, crystalline-like particles, which is consistent with observations in a previous work.[65] The TEM image of the nanocomposite of CND and CdS NPs is shown in Fig. S8c. The nanodots and CdS NPs are evenly distributed. The average particle size of CdS NPs, calculated from the TEM image using ImageJ software, is 7.153 nm. The particle size distribution and the corresponding Gaussian fit are shown in Fig. S8d.

3.5 Scanning electron microscopy of CdS and CND

The SEM image of CNDs is shown in Fig. S9a. The image reveals that the CND particles are granular and tightly packed. This observation has been reported elsewhere.[66] Fig. S9b shows the SEM image of the synthesized CdS NPs; the nanoparticles appear to be spherical and are well distributed in clusters.[52,67] These agglomerations are linked to the small particle sizes of the nanomaterials.

3.6 Energy dispersive X-ray spectroscopy analysis of CdS and CND

The elemental composition and purity of the synthesized materials were checked using EDX. Fig. S10 shows the EDX spectra. Optical absorption peaks at 3–4 keV, attributable to surface plasma resonance, correlate with the metallic CdS nanocrystallites. The EDX spectrum of CdS (Fig. S10a) confirms Cd and S as the major elements. The weight percentages of these elements are 77.8% and 22.2%, relatively comparable to their respective average atomic mass percentages, indicating that the synthesized CdS NPs are pure. The presence of Cl is attributable to byproduct from the synthesis process. The EDX spectrum of CNDs (Fig. S10b) shows C as the predominant

element, confirming the purity of the nanomaterial. As expected, minor elements detected are due to the source (corn cob) used to prepare the CNDs.[68] The EDX spectrum of the nanocomposite (Fig. S10c) confirms the presence of both nanomaterials.

4 Electrochemical and photoelectrochemical characterizations of the developed immunosensors

Electrochemical characterization of the immunosensor was performed under optimized conditions (Fig. S11) using cyclic voltammetry (CV) and electrochemical impedance spectroscopy (EIS) in a 10 mM $[Fe(CN)_6]^{3-/4-}$ redox probe containing 0.1 M KCl. In EIS, the semicircular diameter of the Nyquist plot represents the charge transfer resistance (R_{ct}); the wider it is, the higher the electron transfer resistance, and the smaller it is, the lower the electron transfer resistance.[69] Fig. 1a shows the EIS curves of the fabrication process. Curve (*a*) represents the unmodified electrode, which demonstrates a high R_{ct} of about 111 Ω. This high charge transfer resistance is due to the binders (polymers such as polyvinylidene fluoride, *N*-methyl-2-pyrrolidone, polystyrene, polyaniline and nitrocellulose) used during its production, which impedes electron transfer by blocking electron flow.[70] Modification with CNDs (curve b) lowered the charge transfer resistance to around 101 Ω due to their conductivity and large surface area, which provides adequate sites for electrochemical reactions.[71] Further coating with CdS NPs (curve c) reduced the R_{ct} to about 86 Ω. This further reduction in R_{ct} demonstrates faster electron transfer

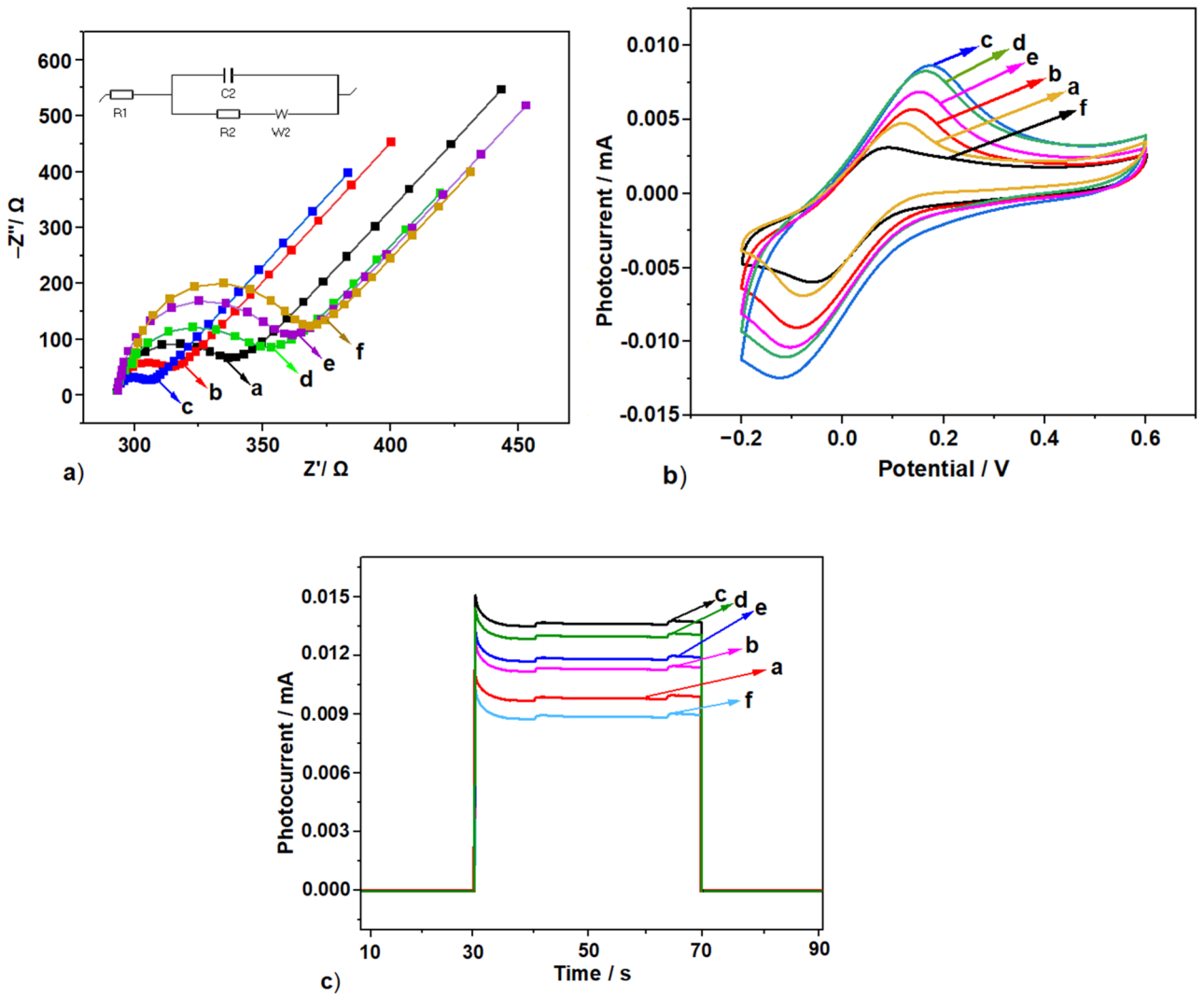

Fig. 1 Stepwise CA 125 immunosensor fabrication process: (a) EIS in the presence of 10 mmol L^{-1} $[Fe(CN)_6]^{3-/4-}$ solution containing 0.1 M KCl; (b) cyclic voltammograms of the fabrication process in the presence of 10 mmol L^{-1} $[Fe(CN)_6]^{3-/4-}$ solution containing 0.1 M KCl; and (c) corresponding photocurrent-time curves in 10 mmol L^{-1} $[Fe(CN)_6]^{3-/4-}$ solution containing 0.1 M KCl and 0.01 M AA. Electrode notations: (a) SPCE, (b) SPCE/CND, (c) SPCE/CND/CdS, (d) SPCE/CND/CdS/NHS–EDC, (e) SPCE/CND/CdS/NHS–EDC/Anti-CA 125, and (f) SPCE/CNDs/CdS/NHS–EDC/anti-CA 125/BSA.

rate and ion diffusion, which is due to the increased surface area provided by CdS NPs and their synergistic interaction with CNDs, enhancing the redox reaction of ferrocyanide molecules.[72] Additional coating with the EDC/NHS complex (curve *d*, 158 Ω) increased R_{ct} due to the insulating effect of the non-conductive organic linker.[73] Subsequent coatings of anti-CA 125 (curve *e*, 193 Ω) and BSA (curve *f*, 270 Ω) on the electrode surface progressively increased R_{ct} and is attributable to the low conductivity and steric hindrance of proteins.[24]

These observations confirm the successful stepwise assembly of the immunosensor. To further validate the fabrication process, cyclic voltammetry was used to analyze the electron transport properties of each modified electrode. Fig. 1b shows the voltammogram recorded during the fabrication process of the CA 125 immunosensor. The bare screen-printed carbon electrode exhibited a low anodic peak current of 0.005 mA and a higher ΔE_p of 229.7 mV (curve *a*) due to its limited light absorption ability, which hinders electron excitation, and the presence of some components such as polymers that impede electron transfer.[70] Upon modification with CND, the peak current improved to approximately 0.007 mA while ΔE_p dropped to 199.2 mV (curve *b*) as a result of the large surface area provided by the CNDs, which enhances the electron transfer reaction of ferrocyanide molecules.[72] Further modification with CdS NPs increased the peak current to 0.0092 mA and decreased ΔE_p to 130.3 mV (curve *c*). This enhancement in photocurrent and reduction in ΔE_p is due to the increased surface area provided by CdS NPs and the matching energy level between CdS NPs and CND, which facilitates charge transfer.[74,75] With the introduction of the EDC/NHS complex, the photocurrent reduced slightly to 0.0086 mA, and ΔE_p became 243.7 mV (curve *d*) due to the insulating effect of the organic linker molecules.[76] With successive immobilization of anti-CA 125 (curve *e*) and BSA (curve *f*), the photocurrent further reduced to 0.0071 and 0.0033 mA, while the ΔE_p further increased to 261.2 and 276.3 mV, respectively. This decrease in photocurrent is due to the insulating properties of biomolecules, which hinder electron transfer,[77] and the increase in ΔE_p

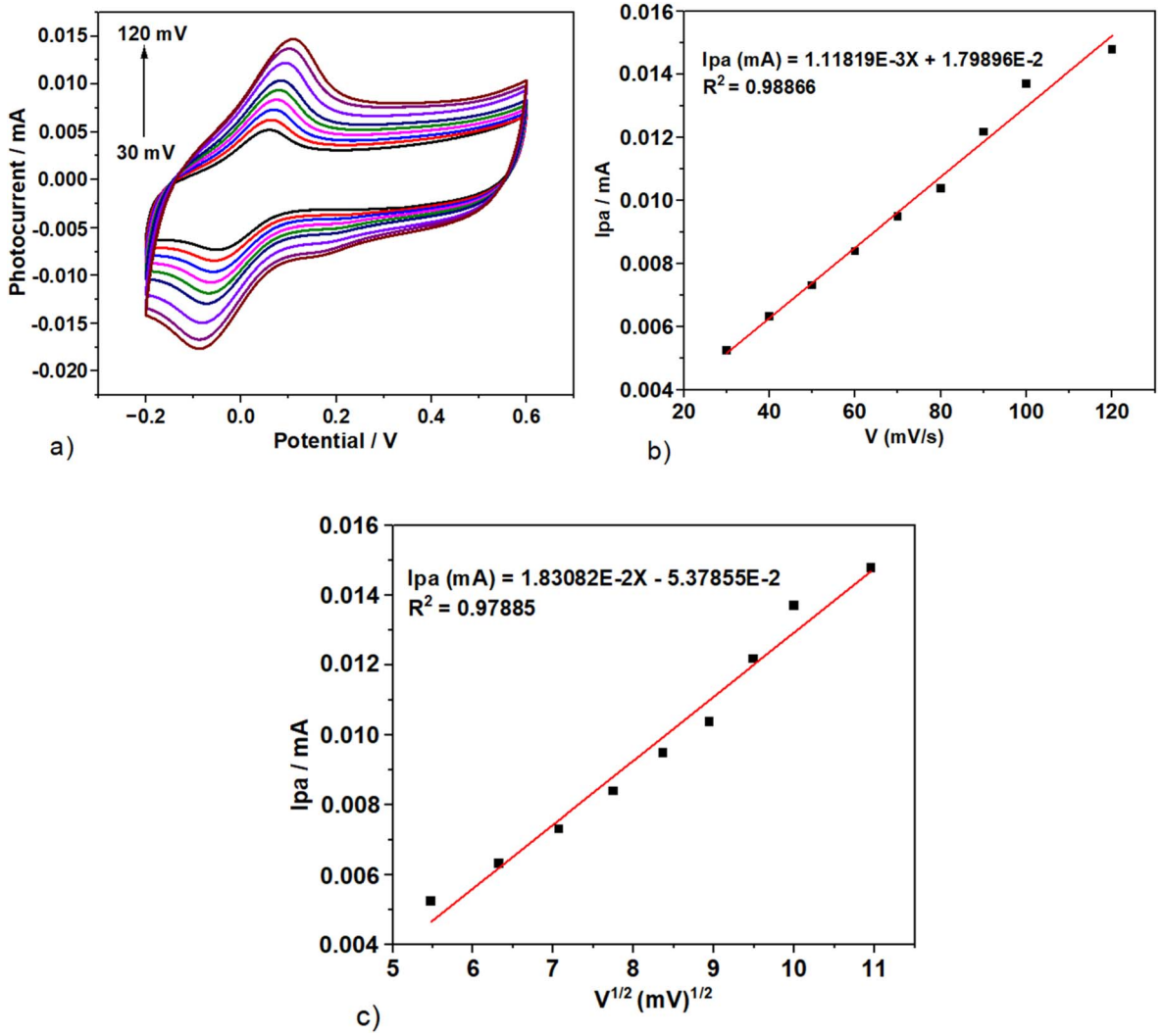

Fig. 2 (a) Cyclic voltammograms at scan rates of 30, 40, 50, 60, 70, 80, 90, 100, and 120 mV s^{-1}; (b) plot of anodic peak current (I_{pa}) *versus* the scan rate (*V*); (c) plot of anodic peak current (I_{pa}) *versus* the square root of the scan rate ($V^{1/2}$).

signifies a lower electron transfer rate.[74] The I_{pa}/I_{pc} ratio at each fabrication stage was close to 1. This suggests that the electrochemical process is reversible and confirms that the reaction is not an adsorption process.[78]

The photocurrent-time response at each fabrication step was further analyzed (Fig. 1 c) to authenticate the successful fabrication process. The bare screen-printed carbon electrode (SPCE) displayed a smaller photocurrent (curve a; 0.0101 mA) due to its limited intrinsic photoactivity.[79] Upon modification with CNDs, the photocurrent increased significantly to approximately 0.0116 mA (curve *b*), attributable to the photoexcitation of electrons from the valence band to the conduction band and their subsequent transfer to CdS under light irradiation.[66] Further modification with CdS NPs increased the photocurrent to 0.0143 mA due to the enhanced electron transfer from the valence band of CdS to its conduction band and their subsequent transfer to the SPCE.[66]

When the electrode surface was modified sequentially with the EDC/NHS complex, anti-CA 125 and BSA, the photocurrent intensity reduced to 0.0135 mA (curve *d*), 0.0124 mA (curve *e*) and 0.00091 mA (curve *f*), respectively. This reduction in photocurrent is attributable to the blocking effect of the materials on electron transfer between ascorbic acid (electron donor) and CdS.[66] These photocurrent trends clearly demonstrate the successful assembly and functionality of the photoelectrochemical immunosensor.

4.1 Effect of scan rate

To investigate the electrochemical reaction mechanism of CA 125 detection, the effect of the scan rate was investigated using CV at scan rates ranging from 30 to 120 mV. The resulting cyclic voltammograms are shown in Fig. 2a. The regression curves of peak current *vs.* scan rate (Fig. 2b) and peak current *vs.* the square root of scan rate (Fig. 2c) show linear relationships, with the following regression equations: I_{pa} (mA) $= 1.11819 \times 10^{-3}x + 1.79896 \times 10^{-2}$ ($R^2 = 0.98866$) and I_{pa} (mA) $= 1.83082 \times 10^{-2}x - 5.37855 \times 10^{-2}$ ($R^2 = 0.97885$), respectively. The slope is close to the theoretical value (0.5) for a diffusion-controlled reaction mechanism; hence, the type of reaction at the electrode/reactant interface is diffusion-controlled.[80]

The relationship between the anodic peak current and the square root of the scan rate was used to determine the electrochemically active surface area of the unmodified and modified electrodes in 10 mM $[Fe(CN)_6]^{3-}/[Fe(CN)_6]^{4-}$ solution using the Randles–Sevcik equation.[81]

$$I_p = 2.691 \times 10^5 n^{3/2} D^{1/2} V^{1/2} AC, \quad (2)$$

where A is the electrochemical activity surface area, C is the electrolyte concentration (0.01 M), D is the diffusion coefficient ($D = 7.6 \times 10^{-6}$ cm^2 s^{-1}), v is the scan rate (V s^{-1}) (60 mV s^{-1}), I_p is the peak current (A), and n is the number of electrons involved in the charge transfer ($n = 1$). The effective surface area was determined to be 0.0181 cm^2 for the bare SPCE, 0.08633 cm^2 for the SPCE/CND electrode and 0.1054 cm^2 for the SPCE/CND/CdS electrode. This improvement in active surface area is due to the extremely high surface area-to-volume ratio of the nanomaterials, which promotes fast electron transfer kinetics and ion diffusion within the SPCE/CND/CdS system.[72]

4.2 Detection of CA 125

The detection of CA 125 was carried out using differential pulse voltammetry (DPV) under optimized experimental conditions. The photocurrent response of the developed BSA/anti-CA 125/EDC-NHS/CdS/CND/SPCE immunosensor towards detection of various concentrations of CA 125 (100, 10, 0.1, 0.01, 0.001, 0.0001 and 0.00001 μg mL^{-1}) is shown in Fig. 3.

The photocurrent intensity decreased as the concentration of CA 125 increased, which is consistent with the literature.[77,82] This decrease in photocurrent is due to the inhibitory effect of the increased concentration of CA 125 antigen on the immunosensor platform.[77] The inset (Fig. 3) shows the calibration curve, which shows good linearity between CA 125 concentration and the peak photocurrent change ($\Delta I_p = I_0 - I$), where 'I_0' is the anodic peak current before CA 125 biorecognition event, and 'I' is the anodic peak current after CA 125 biorecognition. This was observed in the range of 100 to 0.00001 μg mL^{-1}, with a linear regression equation of ΔI_p (A) $= 5.2979 \times 10^{-3} X + 3.14227 \times 10^{-3}$ ($R^2 = 0.97656$) and a low limit of detection (LOD) of 0.0000027 μg mL^{-1} (S/N = 3). This LOD is below the healthy human CA 125 concentration of 35 μg mL^{-1}.[83] Hence, this sensor can detect lower and higher concentrations of CA 125 relative to healthy human serum concentrations. Therefore, the immunosensor has the potential for early detection of gynaecologic malignancies including ovarian cancer (when the CA 125 concentration is low) and for monitoring treatment progress (when CA 125 concentration is high).

The proposed CA 125 immunosensor was compared with other reported immunosensors for CA 125 detection, as listed in Table 1. The limit of detection and linear range achieved in this study surpass those reported in most of the works,

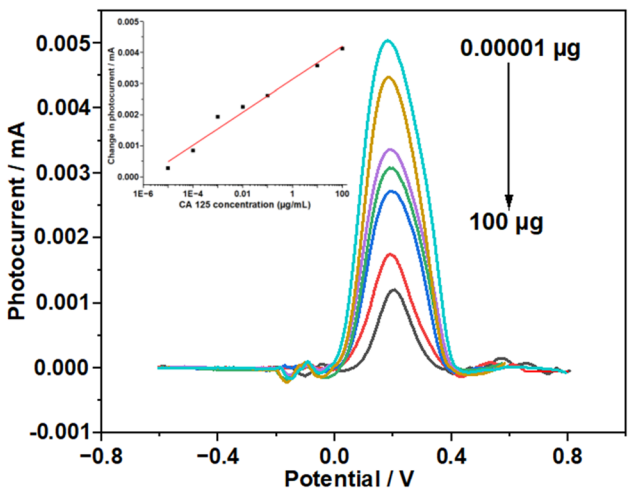

Fig. 3 The DPV voltammograms (in the presence of light) of the fabricated immunosensor incubated with different CA 125 concentrations: 100, 10, 0.1, 0.01, 0.001, 0.0001 and 0.00001 μg mL^{-1} of CA 125 in 10 mmol L^{-1} $[Fe(CN)_6]^{3-/4-}$ solution containing 0.1 M KCl and 0.01 M AA.

Table 1 Comparison of the present study with other reported methods for CA 125 detection[a,b,c]

Sensing platform	Analytical method	Linear range (μg mL^{-1})	LOD (μg mL^{-1})	References
PANI/Gr	EC	0.00092 to 15.2	0.923	83
ZnO NRs–Au NPs	EC	2.5 to 1000	2.5	84
CdS/Bi_2S_3/NiS	PEC	0.000001 to 0.05	0.00000085	24
FA@H-PANI@CS-HCl/Ag@Co_3O_4	EC	0.000001 to 0.025	0.00000025	85
CdS/CND	PEC	100 to 0.00001	0.0000027	This work

[a] EC: electrochemical sensing; PEC: photoelectrochemical sensing; PANI: polyaniline; Gr: graphene. [b] NRs: nanorods; H-PANI: HCl-doped PANI; FA: ferrocenecarboxylic acid; CS: chitosan. [c] NiS: nickel sulfide.

demonstrating the superior performance and sensitivity of the proposed PEC immunosensor for CA 125 detection.

4.3 Selectivity/sensitivity studies

In the selectivity study, the developed CA 125 immunosensor was incubated with various interfering substances, including of 10 μg mL^{-1} PSA, CEA, D-glucose and HE4. The developed immunosensor exhibited excellent selectivity for CA 125, as seen by the significantly high photocurrent generated for the CA 125 antigen (10 μg mL^{-1}) compared to the interfering substances (<23% interference) (Fig. 4a). These results show that the immunosensor possesses good selectivity for CA 125.

4.4 Reproducibility studies

Fig. 4b shows the results of the reproducibility study, which was carried out using five identical immunosensors each to detect

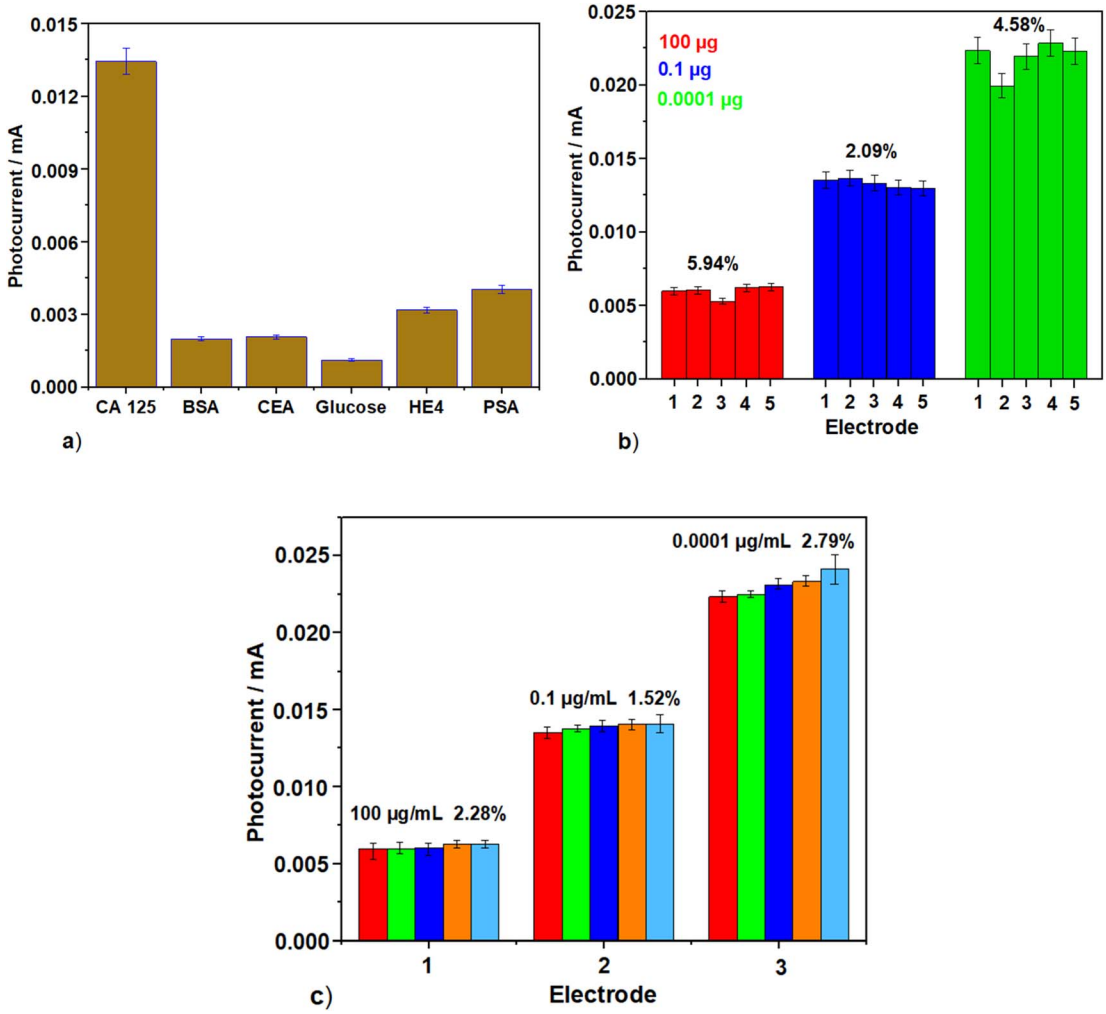

Fig. 4 (a) Selectivity test in the presence of interferents; (b) reproducibility studies; (c) repeatability studies by DPV in the presence of 10 mmol L^{-1} $[Fe(CN)_6]^{3-/4-}$ solution containing 0.1 M KCl and 0.01 M AA.

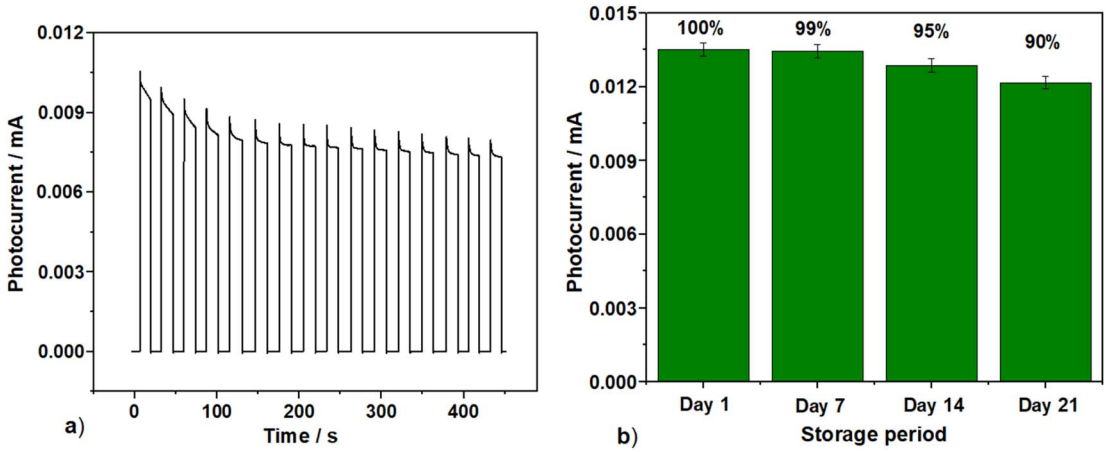

Fig. 5 (a) Stability test under several on/off irradiation cycles of 15 seconds each. (b) Stability test of the CA 125 immunosensor over 21 days for the detection of 0.1 μg CA 125 antigen by DPV in the presence of 10 mmol L^{-1} $[Fe(CN)_6]^{3-/4-}$ solution containing 0.1 M KCl and 0.01 M ascorbic acid.

CA 125 at concentrations of 100, 0.1 and 0.0001 μg mL^{-1}. The relative standard deviation was <6%, indicating excellent reproducibility.

4.5 Repeatability studies

Repeatability studies were performed by running the developed immunosensor for five runs at time interval of 20 s each for the detection of CA 125 antigen at concentrations of 100, 0.1 and 0.0001 μg mL^{-1} (Fig. 4c); the relative standard deviations were 2.28%, 1.52% and 2.79%, respectively. These values are very low, which signifies good repeatability.

4.6 Stability studies

The short-term (15 seconds) and long-term (21 days) stability of the PEC immunosensor was studied by detecting 0.1 μg of CA 125. For the 15-second stability test, photocurrent responses were recorded over multiple on/off irradiation cycles for 450 seconds at an interval of 15 seconds (Fig. 5a). The photocurrent decreased progressively up to around 100 s before stabilization, indicating that the developed PEC immunosensor exhibits a stable photocurrent response for CA 125 detection. The 21-day storage stability was also evaluated by storing the immunosensors at 4 °C for 7, 14, and 21 days, after which the photocurrent intensity was evaluated using DPV. Fig. 5b shows the photocurrent responses of the immunosensors. The immunosensor retained 99%, 95% and 90% of its initial photocurrent on Day 7, 14 and 21, respectively, which shows a gradual fluctuation over the storage period. With only 10% signal loss after 21 days of storage, the immunosensor demonstrates good stability. The slight reduction in photocurrent is caused by some loss of sensor activity over the storage time, which might be linked to minor degradation of biomolecules and environmental factors during storage.[86] Generally, this finding suggests that the immunosensor can be used for long durations, making it suitable for extended practical use.

4.7 Serum sample analysis

To validate the practical application of the immunosensor, fetal bovine serum was used in this study. The serum sample was diluted in phosphate-buffered saline solution (0.1 M; pH, 7.4) at a dilution ratio of 1 : 100 and examined using the standard dilution method.[82] CA 125 antigen was spiked into the diluted serum samples at concentrations of 10, 0.1 and 0.0001 μg mL^{-1}, which were then analyzed three times each. Table 2 shows the results obtained. The percentage relative standard deviations (4.09, 4.27 and 1.26) and percentage recoveries (95.2, 96 and 99%, respectively) confirm possible real-time clinical application of the developed immunosensor.

The developed PEC immunosensor has the advantages of being cost-effective with simple preparation steps and a quick response time of 30 min. It is also very sensitive towards the detection of very low concentrations of CA 125. It may, however, be susceptible to biomolecular degradation because of the significant reduction in signal over a long period of time. Additionally, the potential toxicity of CdS remains a concern.

Table 2 Determination of CA 125 antigen in fetal bovine serum (dilution factor = 1 : 100)

Amount of CA 125 antigen added (μg mL^{-1})	CA 125 antigen detected (μg mL^{-1})	Standard error of mean	RSD (% $n = 3$)	Recovery (%)
10	9.929, 9.635, 8.996	0.225	4.09	95.2
0.1	0.091, 0.101, 0.097	0.002	4.27	96
0.0001	0.000098, 0.000101, 0.000099	0.0000007	1.26	99

5 Conclusion

In summary, an SPCE/CND/CdS NP-based immunosensor was developed and used for the detection of CA 125. The interaction between CND and CdS NPs and their matching energy levels improved the sensitivity of the sensor. The sensor detected CA 125 over a range of 100 to 0.00001 μg mL^{-1} with a low detection limit of 0.0000027 μg mL^{-1}. The immunosensor exhibited excellent sensitivity, repeatability and reproducibility with good short- and long-term stability. It also performed well in detecting CA 125 in the serum environment with a good percentage recovery. Therefore, the developed sensing platform can be used in real-time biosensing of CA 125 and other disease-related biomarkers.

Conflicts of interest

There are no conflicts to declare.

Data availability

Access to the data generated from this work is not restricted and will be publicly available.

Supplementary information: materials and instrumentation; Syntheses and characterizations of materials; Optimisation experiments. See DOI: **https://doi.org/10.1039/d5ra05359e**.

References

1 CANSA Ovarian cancer. **https://cansa.org.za/ovarian-cancer/**, accessed 20th June, 2025.
2 A. S. O'Shea, Clinical staging of ovarian cancer, in *Ovarian Cancer: Methods and Protocols*, Springer, 2021, pp. 3–10.
3 B. M. Reid, J. B. Permuth and T. A. Sellers, Epidemiology of ovarian cancer: a review, *Cancer Biol. Med.*, 2017, **14**(1), 9–32.
4 J. M. Liberto, S.-Y. Chen, I.-M. Shih, T.-H. Wang, T.-L. Wang and T. R. Pisanic, Current and emerging methods for ovarian cancer screening and diagnostics: a comprehensive review, *Cancers*, 2022, **14**(12), 2885.
5 M. Montagnana, M. Benati and E. Danese, Circulating biomarkers in epithelial ovarian cancer diagnosis: from present to future perspective, *Ann. Transl. Med.*, 2017, **5**(13), 276.
6 F. Weiland, K. Martin, M. K. Oehler and P. Hoffmann, Deciphering the molecular nature of ovarian cancer biomarker CA 125, *Int. J. Mol. Sci.*, 2012, **13**(8), 10568–10582.
7 A. Lauby, O. Colomban, P. Corbaux, J. Peron, L. Van Wagensveld, W. Gertych, N. Bakrin, P. Descargues, J. Lopez and V. Kepenekian, The increasing prognostic and predictive roles of the tumor primary chemosensitivity assessed by CA-125 elimination rate constant K (KELIM) in ovarian cancer: A narrative review, *Cancers*, 2021, **14**(1), 98.
8 C. A. Iyoke, L. Lucky, G. O. Ugwu, E. Ezugwu, L. Ajah and R. C. Onoh, Ovarian cancer screening: the role and drawbacks of ultrasonography and feasibility in low resource settings, *Am. J. Clin. Med. Res.*, 2015, **3**(1), 1–8.
9 D. R. Nebgen, K. H. Lu and R. C. Bast, Novel approaches to ovarian cancer screening, *Curr. Oncol. Rep.*, 2019, **21**, 1–11.
10 I. Mendes, M. das Neves and F. Lopes, Biosensor applicability in breast cancer diagnosis, *Int. J. Biosens. Bioelectron.*, 2019, **5**(4), 125–130.
11 T. Mavrič, M. Benčina, R. Imani, I. Junkar, M. Valant, V. Kralj-Iglič, and A. Iglič, Electrochemical biosensor based on TiO2 nanomaterials for cancer diagnostics, in *Advances in Biomembranes and Lipid Self-Assembly*, Elsevier, 2018, vol. 27, pp. 63–105.
12 H. Sohrabi, N. Bolandi, A. Hemmati, S. Eyvazi, S. Ghasemzadeh, B. Baradaran, F. Oroojalian, M. R. Majidi, M. de la Guardia and A. Mokhtarzadeh, State-of-the-art cancer biomarker detection by portable (Bio) sensing technology: A critical review, *Microchem. J.*, 2022, **177**, 107248.
13 E. U. Ekwujuru, A. M. Olatunde, M. J. Klink, C. C. Ssemakalu, M. M. Chili and M. G. Peleyeju, Electrochemical and Photoelectrochemical Immunosensors for the Detection of Ovarian Cancer Biomarkers, *Sensors*, 2023, **23**(8), 4106.
14 L. Wang, H. Wang, C. Tizaoui, Y. Yang, J. Ali and W. Zhang, Endocrine disrupting chemicals in water and recent advances on their detection using electrochemical biosensors, *Sens. Diagn.*, 2023, **2**(1), 46–77.
15 M. Ahmad, M. Hasan, N. Tarannum and S. Ahmed, Recent advances in optical and photoelectrochemical nanobiosensor technology for cancer biomarker detection, *Biosens. Bioelectron.:X*, 2023, **14**, 100375.
16 S. Tian, Z. Yu, Y. Wang, S. Chen, M. Li and D. Tang, Crystal facet engineering modulated electron transfer mechanisms: a self-powered photoelectrochemical sensing platform for noninvasive detection of uric acid, *Anal. Chem.*, 2025, **97**(17), 9518–9526.
17 H. Wang, J. Tang, X. Wan, X. Wang, Y. Zeng, X. Liu and D. Tang, Mechanism exploration of the photoelectrochemical immunoassay for the integration of radical generation with self-quenching, *Anal. Chem.*, 2024, **96**(38), 15503–15510.
18 Y. Gao, J. Tang, Q. Zhou, Z. Yu, D. Wu and D. Tang, Excited-state intramolecular proton transfer-driven photon-gating for photoelectrochemical sensing of CO-releasing molecule-3, *Anal. Chem.*, 2024, **96**(12), 5014–5021.
19 L. Lu, R. Zeng, Q. Lin, X. Huang and D. Tang, Cation exchange reaction-mediated photothermal and polarity-switchable photoelectrochemical dual-readout biosensor, *Anal. Chem.*, 2023, **95**(44), 16335–16342.
20 L. Li, Y. Weng, C. Sun, Y. Peng and Q. Xie, Photoelectrochemical immunoassay of alpha-fetoprotein based on a SnO 2/In 2 S 3 heterojunction and an enzyme-catalyzed precipitation strategy, *Sens. Diagn.*, 2023, **2**(5), 1249–1255.
21 B. Zhang, Y. Jia, J. Wang, X. Hu, Z. Zhao and Y. Cheng, Cysteine-assisted photoelectrochemical immunoassay for the carcinoembryonic antigen by using an ITO electrode modified with C 3 N 4-BiOCl semiconductor and CuO nanoparticles as antibody labels, *Microchim. Acta*, 2019, **186**, 1–7.

22 J. B. Kaushal, P. Raut and S. Kumar, Organic electronics in biosensing: a promising frontier for medical and environmental applications, *Biosensors*, 2023, **13**(11), 976.
23 C. Liao, Y. Xiong, Y. Fu, X. Chen and L. G. Occhipinti, Organic semiconductors based wearable bioelectronics, *Wearable Electron.*, 2025, **2**, 23–39.
24 S. Wang, J. Yuan, C. Wang, T. Wang, F. Zhao and B. Zeng, CdS/Bi2S3/NiS ternary heterostructure-based photoelectrochemical immunosensor for the sensitive detection of carbohydrate antigen 125, *Anal. Chim. Acta*, 2024, **1312**, 342765.
25 H. Xue, J. Zhao, Q. Zhou, D. Pan, Y. Zhang, Y. Zhang and Y. Shen, Boosting the sensitivity of a photoelectrochemical immunoassay by using SiO2@ polydopamine core–shell nanoparticles as a highly efficient quencher, *ACS Appl. Nano Mater.*, 2019, **2**(3), 1579–1588.
26 K. Zou, Y. Fu, R. Yang, X. Zhang, C. Du and J. Chen, CuO–ZnO heterojunction derived from Cu2+-doped ZIF-8: A new photoelectric material for ultrasensitive PEC immunoassay of CA125 with near-zero background noise, *Anal. Chim. Acta*, 2020, **1099**, 75–84.
27 Y. Gao, Z. Yu, L. Huang, Y. Zeng, X. Liu and D. Tang, Photoinduced electron transfer modulated photoelectric signal: toward an organic small molecule-based photoelectrochemical platform for formaldehyde detection, *Anal. Chem.*, 2023, **95**(23), 9130–9137.
28 R. Zeng, J. Xu, T. Liang, M. Li and D. Tang, Photocurrent-polarity-switching photoelectrochemical biosensor for switching spatial distance electroactive tags, *ACS Sens.*, 2023, **8**(1), 317–325.
29 G. He, Y. Zhang and Q. He, MoS2/CdS heterostructure for enhanced photoelectrochemical performance under visible light, *Catalysts*, 2019, **9**(4), 379.
30 N. Qutub, P. Singh, S. Sabir, S. Sagadevan and W.-C. Oh, Enhanced photocatalytic degradation of Acid Blue dye using CdS/TiO2 nanocomposite, *Sci. Rep.*, 2022, **12**(1), 5759.
31 Q. Wu, L. Huang, Z. Li, W. An, D. Liu, J. Lin, L. Tian, X. Wang, B. Liu and W. Qi, The potential application of raw cadmium sulfide nanoparticles as CT photographic developer, *Nanoscale Res. Lett.*, 2016, **11**, 1–8.
32 P. T. Poojitha, R. Dhanalakshmi, M. R. Karim, S. J. An, K. Madhusudana Rao, S. P. R. Mallem and Y. L. Kim, Effective CdS:(Ce, Ga) Nanoparticles for Photocatalytic H2 Production Under Artificial Solar Light Exposer, *J. Compos. Sci.*, 2025, **9**(1), 34.
33 S. Smith, K. Goodge, M. Delaney, A. Struzyk, N. Tansey and M. Frey, A Comprehensive Review of the Covalent Immobilization of Biomolecules onto Electrospun Nanofibers, *Nanomaterials*, 2020, **10**(11), 2142.
34 M. Pourmadadi, A. Moammeri, A. Shamsabadipour, Y. F. Moghaddam, A. Rahdar and S. Pandey, Application of various optical and electrochemical nanobiosensors for detecting cancer antigen 125 (CA-125): a review, *Biosensors*, 2023, **13**(1), 99.
35 A. Sciortino, A. Cannizzo and F. Messina, Carbon nanodots: a review—from the current understanding of the fundamental photophysics to the full control of the optical response, *C*, 2018, **4**(4), 67.
36 O. Mkhari, T. D. Ntuli, N. J. Coville, E. N. Nxumalo and M. S. Maubane-Nkadimeng, Supported carbon-dots: A review, *J. Lumin.*, 2023, **255**, 119552.
37 S. Gengan, H. A. Murthy, M. Sillanpää and T. Nhat, Carbon dots and their application as photocatalyst in dye degradation studies-Mini review, *Results Chem.*, 2022, **4**, 100674.
38 A. Mei, Z. Xu, X. Wang, Y. Liu, J. Chen, J. Fan and Q. Shi, Photocatalytic materials modified with carbon quantum dots for the degradation of organic pollutants under visible light: A review, *Environ. Res.*, 2022, **214**, 114160.
39 S. Das, B. Saha, M. Tiwari and D. K. Tiwari, Diagnosis of cancer using carbon nanomaterial-based biosensors, *Sens. Diagn.*, 2023, **2**(2), 268–289.
40 N. Soni, S. Singh, S. Sharma, G. Batra, K. Kaushik, C. Rao, N. C. Verma, B. Mondal, A. Yadav and C. K. Nandi, Absorption and emission of light in red emissive carbon nanodots, *Chem. Sci.*, 2021, **12**(10), 3615–3626.
41 H. Yu, R. Shi, Y. Zhao, G. I. Waterhouse, L. Z. Wu, C. H. Tung and T. Zhang, Smart utilization of carbon dots in semiconductor photocatalysis, *Adv. Mater.*, 2016, **28**(43), 9454–9477.
42 L. Cui, X. Ren, M. Sun, H. Liu and L. Xia, Carbon dots: Synthesis, properties and applications, *Nanomaterials*, 2021, **11**(12), 3419.
43 A. B. Patil, P. L. Chaudhary and P. V. Adhyapak, Carbon dots–cadmium sulfide quantum dots nanocomposite for 'on–off' fluorescence sensing of chromium (vi) ions, *RSC Adv.*, 2024, **14**(18), 12923–12934.
44 M. M. Rahman, In-situ preparation of cadmium sulphide nanostructure decorated CNT composite materials for the development of selective benzaldehyde chemical sensor probe to remove the water contaminant by electrochemical method for environmental remediation, *Mater. Chem. Phys.*, 2020, **245**, 122788.
45 A. O. Idris, N. Mabuba and O. A. Arotiba, An exfoliated graphite-based electrochemical immunosensor on a dendrimer/carbon nanodot platform for the detection of carcinoembryonic antigen cancer biomarker, *Biosensors*, 2019, **9**(1), 39.
46 J. D. Tinkler, A. Scacchi, M. Argaiz, R. Tomovska, A. J. Archer, H. Willcock and I. Martín-Fabiani, Effect of particle interactions on the assembly of drying colloidal mixtures, *Langmuir*, 2022, **38**(18), 5361–5371.
47 M. Hayat, E. Saepudin, Y. Einaga and T. A. Ivandini, Cds nanoparticle-based biosensor development for aflatoxin determination, *Int. J. Technol.*, 2019, **10**(4), 787–797.
48 J. Mintseris and S. P. Gygi, High-density chemical cross-linking for modeling protein interactions, *Proc. Natl. Acad. Sci. U. S. A.*, 2020, **117**(1), 93–102.
49 J. D. Walters, S. S. Gill and J. J. Mercuri, Ethanol-mediated compaction and cross-linking enhance mechanical properties and degradation resistance while maintaining cytocompatibility of a nucleus pulposus scaffold, *J. Biomed. Mater. Res., Part B*, 2019, **107**(8), 2488–2499.

50 E. Ryskina, F. Gilmiyarova, B. Ahmedzhanov, and N. Maksimuk, in *The Effect of Ethanol on Protein-Ligand Interactions, IOP Conference Series: Earth and Environmental Science*, IOP Publishing, 2021, p. 032111.
51 Y. Feng, X. Ma, B. Kong, Q. Chen and Q. Liu, Ethanol induced changes in structural, morphological, and functional properties of whey proteins isolates: Influence of ethanol concentration, *Food Hydrocolloids*, 2021, **111**, 106379.
52 S. Kumar and J. Sharma, Stable phase CdS nanoparticles for optoelectronics: a study on surface morphology, structural and optical characterization, *Mater. Sci.*, 2016, **34**(2), 368–373.
53 A. Haile, Fourier transform infrared spectroscopy (ftir) study of cadmium sulfide (cds) thin film prepared by chemical rute, *Int. J. Sci. Eng. Res.*, 2020, **11**, 1539.
54 T. Senasu, N. Ruengchai, S. Khamdon, N. Lorwanishpaisarn and S. Nanan, Hydrothermal synthesis of cadmium sulfide photocatalyst for detoxification of azo dyes and ofloxacin antibiotic in wastewater, *Molecules*, 2022, **27**(22), 7944.
55 M. Zulfajri, S. Dayalan, W.-Y. Li, C.-J. Chang, Y.-P. Chang and G. G. Huang, Nitrogen-doped carbon dots from averrhoa carambola fruit extract as a fluorescent probe for methyl orange, *Sensors*, 2019, **19**(22), 5008.
56 H. K. Chung, V. Wongso and N. S. Sambudi, Isnaeni, Biowaste-derived carbon dots/hydroxyapatite nanocomposite as drug delivery vehicle for acetaminophen, *J. Sol-Gel Sci. Technol.*, 2020, **93**, 214–223.
57 P. K. Yadav, S. Chandra, V. Kumar, D. Kumar and S. H. Hasan, Carbon quantum dots: synthesis, structure, properties, and catalytic applications for organic synthesis, *Catalysts*, 2023, **13**(2), 422.
58 S. Mura, R. Ludmerczki, L. Stagi, S. Garroni, C. M. Carbonaro, P. C. Ricci, M. F. Casula, L. Malfatti and P. Innocenzi, Integrating sol-gel and carbon dots chemistry for the fabrication of fluorescent hybrid organic-inorganic films, *Sci. Rep.*, 2020, **10**(1), 4770.
59 A. Shivashankarappa and K. Sanjay, Study on biological synthesis of cadmium sulfide nanoparticles by Bacillus licheniformis and its antimicrobial properties against food borne pathogens, *Nanosci. Nanotechnol. Res.*, 2015, **3**(1), 6–15.
60 A. K. Verma, P. Chandra, A. Srivastava and R. Shukla, Optoelectronic studies of commercially and lab prepared cadmium sulfide chalcogenide, *Res. Rev. J. Mater. Sci.*, 2017, **5**(2), 28–34.
61 R. A. Devi, M. Latha, S. Velumani, G. Oza, P. Reyes-Figueroa, M. Rohini, I. Becerril-Juarez, J.-H. Lee and J. Yi, Synthesis and characterization of cadmium sulfide nanoparticles by chemical precipitation method, *J. Nanosci. Nanotechnol.*, 2015, **15**(11), 8434–8439.
62 J. Abraham, B. Jose, A. Jose, and S. Thomas, Characterization of green nanoparticles from plants, in *Phytonanotechnology*, Elsevier, 2020, pp. 21–39.
63 A. Sekar, R. Yadav and N. Basavaraj, Fluorescence quenching mechanism and the application of green carbon nanodots in the detection of heavy metal ions: a review, *New J. Chem.*, 2021, **45**(5), 2326–2360.
64 A. Banger, S. Gautam, S. Jadoun, N. K. Jangid, A. Srivastava, I. N. Pulidindi, J. Dwivedi and M. Srivastava, Synthetic methods and applications of carbon nanodots, *Catalysts*, 2023, **13**(5), 858.
65 A. Regmi, Y. Basnet, S. Bhattarai and S. K. Gautam, Cadmium sulfide nanoparticles: synthesis, characterization, and antimicrobial study, *J. Nanomater.*, 2023, **2023**(1), 8187000.
66 X. Xie, D. Wu, H. Wu, C. Hou, X. Sun, Y. Zhang, R. Yu, S. Zhang, B. Wang and W. Du, Dielectric parameters of activated carbon derived from rosewood and corncob, *J. Mater. Sci.: Mater. Electron.*, 2020, **31**, 18077–18084.
67 A. Dumbrava, C. Badea, G. Prodan and V. Ciupina, Synthesis and characterization of cadmium sulfide obtained at room temperature, *Chalcogenide Lett.*, 2010, **7**(2), 111–118.
68 A. I. Anukam, B. P. Goso, O. O. Okoh and S. N. Mamphweli, Studies on characterization of corn cob for application in a gasification process for energy production, *J. Chem.*, 2017, **2017**(1), 6478389.
69 D. Ribeiro and J. Abrantes, Application of electrochemical impedance spectroscopy (EIS) to monitor the corrosion of reinforced concrete: A new approach, *Constr. Build. Mater.*, 2016, **111**, 98–104.
70 W. T. Wahyuni, B. R. Putra, A. Fauzi, D. Ramadhanti, E. Rohaeti and R. Heryanto, A brief review on fabrication of screen-printed carbon electrode: materials and techniques, *Indones. J. Chem. Res.*, 2021, **8**(3), 210–218.
71 Y. Zhai, B. Zhang, R. Shi, S. Zhang, Y. Liu, B. Wang, K. Zhang, G. I. Waterhouse, T. Zhang and S. Lu, Carbon dots as new building blocks for electrochemical energy storage and electrocatalysis, *Adv. Energy Mater.*, 2022, **12**(6), 2103426.
72 H. M. Saleh and A. I. Hassan, Synthesis and characterization of nanomaterials for application in cost-effective electrochemical devices, *Sustainability*, 2023, **15**(14), 10891.
73 N. H. Masód, S. Azhari and S. S. Othman, Optimization of newly fabricated laccase biosensor based on single-walled carbon nanotubes for tyramine detection, *J. Teknol.*, 2024, **86**(5), 113–120.
74 Y. Yang, S. Niu, D. Han, T. Liu, G. Wang and Y. Li, Progress in developing metal oxide nanomaterials for photoelectrochemical water splitting, *Adv. Energy Mater.*, 2017, **7**(19), 1700555.
75 J. Bhattacharjee and S. Roy, A review on photocatalysis and nanocatalysts for advanced organic synthesis, *Hybrid Adv.*, 2024, 100268.
76 Y. Yang, X. Wang, and B. Hsiao, in *Preparation of Thin Film Nanofibrous Composite NF Membrane Based on EDC/NHS Modified PAN-AA Nanofibrous Substrate*, IOP Conference Series: Materials Science and Engineering, IOP Publishing, 2016, p. 012047.
77 H. Wang, Y. Wang, Y. Zhang, Q. Wang, X. Ren, D. Wu and Q. Wei, Photoelectrochemical immunosensor for detection of carcinoembryonic antigen based on 2D TiO2 nanosheets and carboxylated graphitic carbon nitride, *Sci. Rep.*, 2016, **6**(1), 27385.

78 M. Abdallah, A. Alharbi, M. Morad, A. M. Hameed, S. S. Al-Juaid, N. Foad and E. Mabrouk, Electrochemical studies and the electrode reaction mechanism of ferrocene and naphthoquinones in microemulsion Medium at GC electrode, *Int. J. Electrochem. Sci.*, 2020, **15**(7), 6522–6548.

79 R. M. Silva, A. D. da Silva, J. R. Camargo, B. S. de Castro, L. M. Meireles, P. S. Silva, B. C. Janegitz and T. A. Silva, Carbon nanomaterials-based screen-printed electrodes for sensing applications, *Biosensors*, 2023, **13**(4), 453.

80 D. D. Yadav, A. Kumar, R. Jha and S. Singh, Diffusion Controlled Electrochemical Behavior of Mn Doped Nickel Oxide Nanoparticles for Electrodes in Supercapacitor Applications, *ECS J. Solid State Sci. Technol.*, 2025, **14**(7), 077005.

81 H. Mliki, M. Echabaane, A. Rouis, J. M. El Ghoul, F. Bessueille, D. Ayed and N. Jaffrezic-Renault, Highly electroactive Co–ZnO/GO nanocomposite: Electrochemical sensing platform for oxytetracycline determination, *Heliyon*, 2024, **10**(9), e30265.

82 F. O. Olorundare, D. S. Sipuka, T. I. Sebokolodi, S. Makaluza, N. Midzi, T. Kodama, O. A. Arotiba and D. Nkosi, An electrochemical immunosensor on a carbon nanofiber/gold nanoparticles platform for the detection of alpha-feto protein cancer biomarker, *Sens. Biosens. Res.*, 2023, **41**, 100574.

83 A. Gazze, R. Ademefun, R. S. Conlan and S. R. Teixeira, Electrochemical impedence spectroscopy enabled CA125 detection; toward early ovarian cancer diagnosis using graphene biosensors, *J. Interdiscip. Nanomed.*, 2018, **3**(2), 82–88.

84 G. Gasparotto, J. P. C. Costa, P. I. Costa, M. A. Zaghete and T. Mazon, Electrochemical immunosensor based on ZnO nanorods-Au nanoparticles nanohybrids for ovarian cancer antigen CA-125 detection, *Mater. Sci. Eng., C*, 2017, **76**, 1240–1247.

85 X. Ren, H. Wang, D. Wu, D. Fan, Y. Zhang, B. Du and Q. Wei, Ultrasensitive immunoassay for CA125 detection using acid site compound as signal and enhancer, *Talanta*, 2015, **144**, 535–541.

86 M. Skruodiene, J. Kovger-Jarosevic, I. Savickaja, J. Juodkazyte and M. Petruleviciene, Feasibility Study of Photoelectrochemical Sensing of Glucose and Urea Using BiVO4 and BiVO4/BiOCl Photoanodes, *Sensors*, 2025, **25**(4), 1260.